




## Insights into the atomic structure of the interface of ferroelectric $\text{Hf}_{0.5}\text{Zr}_{0.5}\text{O}_2$ grown epitaxially on $\text{La}_{2/3}\text{Sr}_{1/3}\text{MnO}_3$

Saúl Estandía <sup>1,\*</sup>, Tengfei Cao,<sup>2,\*</sup> Rohan Mishra <sup>2,‡</sup>, Ignasi Fina,<sup>1</sup> Florencio Sánchez <sup>1</sup> and Jaume Gazquez<sup>1</sup>

<sup>1</sup>*Institut de Ciència de Materials de Barcelona (ICMAB-CSIC), Campus UAB, Bellaterra, 08193 Barcelona, Spain*

<sup>2</sup>*Department of Mechanical Engineering & Materials Science, and Institute of Materials Science & Engineering, Washington University in St. Louis, One Brookings Drive, St. Louis, Missouri 63130, USA*



(Received 13 April 2021; revised 2 June 2021; accepted 9 July 2021; published 28 July 2021)

Epitaxial growth of  $\text{Hf}_{0.5}\text{Zr}_{0.5}\text{O}_2$  (HZO) thin films allows for the stabilization of the metastable orthorhombic phase with robust ferroelectric properties. So far, the ferroelectric phase is most commonly stabilized on perovskite substrates upon insertion of a buffer layer of  $\text{La}_{2/3}\text{Sr}_{1/3}\text{MnO}_3$  (LSMO); however, little is known about the role played by the LSMO buffer layer and the interface between HZO and LSMO. Inspection of a HZO/LSMO/ $\text{SrTiO}_3$  heterostructure by scanning transmission electron microscope imaging and electron energy loss spectroscopy shows that, despite the substantial structural mismatch between HZO and LSMO, the interface between them is relatively sharp spanning  $\sim 2$  atomic layers. The LSMO surface, expected to be mostly  $\text{MnO}_2$  terminated, undergoes a chemical reconstruction consisting of the substitution of the Mn cations by a mixture of Hf/Zr cations. Density functional theory calculations show that the substitution of Mn by Hf on the  $\text{MnO}_2$ -terminated surface of LSMO is energetically favorable, as the higher electronegativity and valence of Hf with respect to Mn balances the surface charge of the  $\text{MnO}_2$  layer.

DOI: [10.1103/PhysRevMaterials.5.074410](https://doi.org/10.1103/PhysRevMaterials.5.074410)

### I. INTRODUCTION

Ferroelectric  $\text{HfO}_2$ -based materials are promising because they are highly compatible with complementary metal-oxide semiconductor (CMOS) fabrication processes, and they exhibit ferroelectricity even at a thickness of only a few unit cells, at which most ferroelectrics become depolarized [1–3]. Since the discovery of ferroelectricity in a metastable phase of Si-doped  $\text{HfO}_2$  [4], numerous advances have been made with  $\text{HfO}_2$ -based materials; for example, tunnel junctions [5–7] and ferroelectric random-access memories [8,9] have been fabricated.  $\text{HfO}_2$ -based materials are generally prepared as polycrystalline films [10], and the metastable ferroelectric phase is stabilized by introducing different dopants or by alloying with other cations [11,12]. Among these variants,  $\text{Hf}_{0.5}\text{Zr}_{0.5}\text{O}_2$  (HZO) has shown especially robust ferroelectric properties [13]. Beyond polycrystalline films, epitaxial films can be particularly useful to controllably tune the ferroelectric properties of the films. Ferroelectric  $\text{HfO}_2$  thin films with different dopants have been grown epitaxially on various substrates such as the fluorite yttria-stabilized zirconia (YSZ) [14–16], Si [17], pyrochlore oxides [18], or perovskites like  $\text{SrTiO}_3$  (STO) [19,20],  $\text{LaAlO}_3$  [21], or  $\text{GdScO}_3$  [22]. On the perovskite substrates, a strained  $\text{La}_{2/3}\text{Sr}_{1/3}\text{MnO}_3$  (LSMO) buffer layer or a similar manganite buffer is generally essential to stabilize the metastable ferroelectric phase [19–21,23], with Nb-doped STO being the only perovskite substrate reported to

permit the stabilization of the orthorhombic phase without the use of manganite buffers [24], as far as we know.

HZO and LSMO have dissimilar structures; the fluoritelike structure of HZO and the perovskite structure of LSMO have a large lattice mismatch and different symmetry, yet HZO is epitaxially stabilized in several phases and orientations when deposited on LSMO. The ferroelectric phase of HZO (o-HZO) is generally attributed to the orthorhombic  $Pca2_1$  structure [25], and it seems that LSMO is crucial to stabilize it. For instance, by excluding the LSMO buffer layer, Lyu *et al.* [17] reported that the growth of HZO on a  $\text{LaNiO}_3$  electrode did not yield ferroelectric o-HZO, even though the lattice parameters of  $\text{LaNiO}_3$  are close to those of LSMO (only 0.5% mismatch). The HZO/LSMO heterointerface studied here, grown on STO, yields o-HZO with (111) orientation, in coexistence with the nonferroelectric monoclinic phase, as has been reported previously [6,22,26]. Domain matching epitaxy has been proposed to explain the stabilization of o-HZO on LSMO electrodes [26], as well as interface reconstructions leading to the formation of a metastable tetragonal phase at the interface [19]. However, the precise atomic structure of the HZO/LSMO heterointerface remains unknown.

Here, we provide insights into the structure and chemistry of the HZO/LSMO interface in a HZO/LSMO/STO heterostructure. By combining scanning transmission electron microscopy (STEM) and density functional theory (DFT) calculations, we reveal that the epitaxial heterointerface is mediated by a coherent interfacial monolayer between the HZO and LSMO structures. This monolayer is formed through a chemical reconstruction of the LSMO termination surface, consisting of the substitution of the Mn of the uppermost  $\text{MnO}_2$  layer of the LSMO [27,28] by a mixture of Hf and Zr. Z-contrast imaging and electron energy loss spectroscopy

\*These authors contributed equally to this work.

†Corresponding author: saul.estandia@gmail.com

‡Corresponding author: rmishra@wustl.edu

(EELS) reveal a lower concentration of Hf/Zr in the first HZO plane and the presence of oxygen vacancies at the interface. DFT calculations indicate that the substitution of Mn on the  $\text{MnO}_2$ -terminated surface of LSMO with Hf, together with oxygen vacancies, contributes to surface charge balance and is energetically favorable, which explains the STEM observations. The nature of the heterointerface that enables the epitaxial growth of ferroelectric o-HZO films grown on perovskites is thus revealed.

## II. EXPERIMENTAL SECTION

### A. Thin film deposition

An epitaxial heterostructure formed by HZO (top layer,  $t = 10$  nm) and LSMO (bottom layer,  $t = 25$  nm) was grown on STO(001). The HZO/LSMO heterostructure was deposited in a single process by pulsed laser deposition (KrF excimer laser). Detailed information on growth conditions and ferroelectric properties is reported elsewhere [20,22].

### B. Ferroelectric characterization

The capacitor measuring configuration was obtained by *ex situ* deposition through stencil masks of top platinum electrodes, 20 nm in thickness and 19  $\mu\text{m}$  in diameter, by direct current magnetron sputtering. The ferroelectric polarization loop was obtained at room temperature in top-bottom configuration by means of an AixACCT TFAAnalyser2000 platform with a pulse frequency of 1 kHz. Leakage contribution was compensated using a dynamic leakage current compensation standard procedure [29,30].

### C. Structural characterization

For the characterization of the HZO interface, STEM images and EELS were acquired with an aberration-corrected Nion UltraSTEM 200, operated at 200 kV and equipped with a fifth-order Nion aberration corrector and with a Gatan Enfium spectrometer. For high-angle annular dark field (HAADF)  $Z$ -contrast imaging, a probe convergence angle of 30 mrad and an annular dark-field detector with an inner angle  $>86$  mrad were used. For EELS, the collection semi-angle was 48 mrad. HAADF images of cross-sectional specimens were recorded as viewed along [100] and [110] zone axes of the substrate. The transmission electron microscopy (TEM) specimens were prepared by the conventional method of cutting-gluing-slicing-polishing (mechanical + ion milling). Regarding the EELS characterization, a  $62 \times 160$ -pixel spectrum image (containing a spectrum for each pixel or probe position) was acquired with an exposure time of 0.1 s per pixel, simultaneously with the HAADF image. Then the chemical maps were obtained after removal of the background, which was fitted to an exponential decay law, and further integration of the intensity within a window starting at the edge energy. This was done for each pixel in the spectrum image. EELS images were typically acquired from relatively thin regions, with thickness values in terms of the inelastic mean free path  $t/\lambda < 0.5$ , and were acquired with an energy dispersion of 1 eV/channel for compositional maps and 0.3 eV/channel for the study of the electronic fine structure.

TABLE I. Bader charges analysis of  $\text{MnO}_2$ -terminated LSMO surface without and with Hf clusters.

Configuration ( $2 \times 2 \text{ MnO}_2$ )	Bader atomic charge ( $e$ )			
	Average surface Mn	Hf	Average surface O	Surface charge
Bare $\text{MnO}_2$ surface	5.40		7.06	2.08
Hf-A	5.49	2.26	7.11	1.10
Hf-E	5.42	1.81	7.08	0.13
HfO-A	5.45	1.90	7.09	1.51
HfO-E	5.50	1.73	7.08	1.45
HfO <sub>2</sub> -A	5.38	1.76	7.03	1.58
HfO <sub>2</sub> -E	5.40	1.75	7.02	1.55

### D. Computational details

We have used DFT calculations to investigate the likelihood of Hf adatoms to substitute Mn atoms at the  $\text{MnO}_2$ -terminated surface of LSMO. We have optimized all our structures using DFT as implemented in the VASP package [31]. The energy cutoff for the plane waves was set at 500 eV. The threshold for energy convergence for the self-consistent loop was set to  $1 \times 10^{-6}$  eV, and the convergence criterion for forces was set to  $0.01 \text{ eV \AA}^{-1}$ . We used projector augmented wave potentials [32] and the generalized gradient approximation within the Perdew-Burke-Ernzerhof parameterization [33] to describe the electron-ion and the electronic exchange-correlation interactions. We used orthogonal slabs of (001)-oriented  $\text{La}_{0.75}\text{Sr}_{0.25}\text{MnO}_3$  having symmetric  $\text{MnO}_2$  termination at both surfaces. The in-plane dimensions of the slab were  $2 \times 2$  times that of a 5-atom perovskite unit cell. The thickness of the slab was 3.5 unit cells. The atoms in the central layer are fixed to their bulk coordinates. We used a vacuum of 30  $\text{\AA}$  to minimize interactions between the slab and its periodic images. The Brillouin zone was sampled by a  $4 \times 4 \times 1$   $k$ -points mesh obtained using the Monkhorst-Pack scheme [34]. We imposed ferromagnetic ordering of Mn atoms, which is the ground state for  $\text{La}_{0.75}\text{Sr}_{0.25}\text{MnO}_3$  and the experimentally used  $\text{La}_{0.66}\text{Sr}_{0.33}\text{MnO}_3$  composition [35]. We imposed the  $a^-b^-c^+$  tilting pattern under Glazer's notation for the  $\text{MnO}_6$  octahedral network [36]. Bader charge of each atom in the terminated layer and valence electrons of each element were applied to analyze surface charge states. For example, for the terminated  $\text{MnO}_2$  surface, the average Bader charge of Mn and O were  $5.4 e$  and  $7.06 e$  (Table I), respectively. For Mn and O elements, their valence electrons are  $7 e$  and  $6 e$ . Therefore, the charge of each  $\text{MnO}_2$  unit is  $(5.4-7)e + (7.06-6) \times 2e = 0.52e$ . There are four  $\text{MnO}_2$  units in the terminated layer, and the total surface charge is  $2.08 e$ . To compare the stability of different  $\text{HfO}_x$  adsorbates on  $\text{MnO}_2$ -terminated LSMO under different growth conditions, we have calculated the adsorbate energy  $\sigma(\text{HfO}_x)$  as a function of the chemical potentials of Hf and O,  $\mu_{\text{Hf}}$  and  $\mu_{\text{O}}$ , respectively:

$$\sigma(\text{HfO}_x) = E_{\text{slab}}(\text{HfO}_x/\text{LSMO}) - E_{\text{slab}}(\text{LSMO}) + \mu_{\text{Hf}} + x\mu_{\text{O}}. \quad (1)$$

Here,  $E_{\text{slab}}(\text{HfO}_x/\text{LSMO})$  is the DFT-calculated energy of  $\text{HfO}_x$  adsorbates in their most stable configuration for each  $x$

on  $\text{MnO}_2$ -terminated LSMO, and  $E_{\text{slab}}(\text{LSMO})$  is the energy of the bare  $\text{MnO}_2$ -terminated LSMO slab. The chemical potentials can vary from Hf-rich (O-poor) conditions to Hf-poor (O-rich conditions). For the former, Hf is assumed to be in equilibrium with bulk Hf metal in hexagonal close-packed phase, while for the latter, oxygen is assumed to be in equilibrium with oxygen gas, which in our case is the DFT energy of an isolated  $\text{O}_2$  molecule in its triplet state. Specifically,  $\mu_{\text{Hf}}$  and  $\mu_{\text{O}}$  for the two conditions are defined as

Hf-rich (O-poor) case:

$$\mu_{\text{Hf}} = E_{\text{bulk}}(\text{Hf}); \quad \mu_{\text{O}} = \frac{1}{2}[E_{\text{bulk}}(\text{HfO}_2) - \mu_{\text{Hf}}], \quad (2)$$

Hf-poor (O-poor) case:

$$\mu_{\text{O}} = \frac{1}{2}E(\text{O}_2); \quad \mu_{\text{Hf}} = E_{\text{bulk}}(\text{HfO}_2) - 2\mu_{\text{O}}. \quad (3)$$

In the above,  $E_{\text{bulk}}(\text{HfO}_2)$  is the energy of  $\text{HfO}_2$  in its ground state (monoclinic phase). Using these, we find that, under Hf-rich conditions,  $\mu_{\text{Hf}} = -9.96$  eV and  $\mu_{\text{O}} = -10.32$  eV; and under Hf-poor conditions,  $\mu_{\text{Hf}} = -21.76$  eV and  $\mu_{\text{O}} = -4.42$  eV. Additionally, as the  $\text{MnO}_2$ -terminated LSMO slab is rich in Mn, we assume that it is in equilibrium with bulk Mn, which adds an additional bound on  $\mu_{\text{O}}$ , as follows:

$$\mu_{\text{Mn}} = E_{\text{bulk}}(\text{Mn}); \quad \mu_{\text{O}} = \frac{1}{2}[E_{\text{bulk}}(\text{MnO}_2) - \mu_{\text{Mn}}], \quad (4)$$

where  $E_{\text{bulk}}(\text{MnO}_2)$  is the energy of  $\beta\text{-MnO}_2$ . Based on this bound, we find that  $-6.92$  eV  $\leq \mu_{\text{O}} \leq -4.42$  eV.

### III. RESULTS AND DISCUSSION

A HZO film was grown epitaxially on a (001)-oriented STO substrate buffered with LSMO. LSMO grows with a cube-on-cube orientation relationship on (001)-oriented STO. As reported elsewhere [22], o-HZO (111)-oriented crystallites coexist with nonferroelectric monoclinic (001)-oriented crystallites in the studied film, both phases being epitaxial to LSMO. Among different bottom electrodes, only LSMO stabilizes the o-HZO phase, while other perovskite electrodes, such as  $\text{LaNiO}_3$  or  $\text{SrRuO}_3$ , only yield monoclinic HZO (m-HZO) [23]. The ferroelectric character of the studied film is revealed by an  $I$ - $V$  curve and the corresponding integrated  $P$ - $V$  loop (see Fig. S1, Supplemental Material [37]), with ferroelectric switching peaks at  $\sim 3$ – $4$  V and remanent polarization of  $\sim 12$   $\mu\text{C}/\text{cm}^2$ . Further macroscopic ferroelectric characterization of this film has been reported elsewhere [22,23]. Herein, we focus on the interface between the ferroelectric o-HZO and the LSMO buffer layer, although the interface between the paraelectric monoclinic phase of HZO and the LSMO buffer was also studied in detail, revealing small differences with the orthorhombic phase (see Figs. S2 and S3, Supplemental Material [37]).

Figures 1(a) and 1(b) show two HAADF or Z-contrast images of the interface between (111) o-HZO and the LSMO layer viewed along the [100] and [110] LSMO zone axis, respectively; consequently, o-HZO is also viewed along two different zone axes. The (111) o-HZO crystallites are twinned on the fourfold LSMO surface, implying that o-HZO grains can grow along either [0-22] or [-211] directions aligned with [110] of LSMO [26]. The o-HZO (111) grain in Fig. 1(a) is not viewed along a major crystallographic direction. As a result, the Z-contrast image shows only bright stripes corresponding

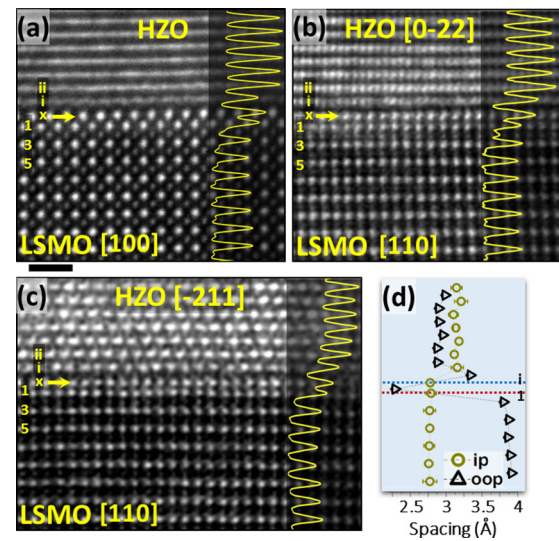


FIG. 1. (a) Z-contrast image of the HZO/LSMO interface along the [100] LSMO zone axis. (b) and (c) Images along the [110] LSMO zone axis, displaying the two possible zone axes (according to the in-plane HZO twins) for the o-HZO grains. No HZO zone axis is close to the substrate [100] zone axis in (a), and as a result, the HZO atomic columns are visible as bright horizontal stripes. The interface monolayer is denoted as  $x$ , and it is indicated by a yellow arrow in the three images, while the first atomic plane of the o-HZO layer is marked with an  $i$ . The row-averaged intensity profiles across the interface (along the out-of-plane direction) are shown on the right side of (a)–(c). Scale bar is 1 nm. (d) In-plane and out-of-plane spacings between planes as seen along [110] of LSMO in the HZO twin variant shown in (c). The distance between consecutive  $\text{La}_{2/3}\text{Sr}_{1/3}\text{O}$  planes is around  $3.9 \pm 0.1$  Å, and that between plane  $x$  and 1 is around  $2.3 \pm 0.1$  Å.

to the out-of-plane (111) cation planes of HZO. On the other hand, the crystal structures of [0-22] and [-211] HZO grains, shown in Figs. 1(b) and 1(c), respectively, become visible when the heterostructure is viewed along the [110] zone axis of the substrate.

We observe rather striking features at the uppermost plane of the LSMO electrode [denoted with an  $x$  and marked with a yellow arrow in Figs. 1(a)–1(c)] and at the lowermost plane of the HZO layer. The intensity in a Z-contrast image is approximately proportional to the squared atomic number ( $Z^2$ ) of the columns. Hence, the heavier cation columns appear brighter than the lighter cation columns. The anion columns (oxygen) are not visible due to the limited dynamic range of the detector. Accordingly, the Z-contrast images shown in Fig. 1 give the expected contrast of an  $\text{AMO}_3$  perovskite, such as the LSMO. The most intense atomic columns correspond to the mixed La/Sr ( $Z_{\text{La}} = 57$ ,  $Z_{\text{Sr}} = 38$ ) sublattice, whereas Mn ( $Z_{\text{Mn}} = 25$ ) atomic columns appear slightly dimmer. While this holds true for both [100] and [110] zone axes, the uppermost plane with LSMO structure (denoted as  $x$ ) shows a more intense atomic column than expected. Had the LSMO buffer layer ended with a  $\text{MnO}_2$  plane, its intensity would have been lower. This is clearly evidenced by tracing the profile intensity across the interface and comparing the intensity of the atomic plane  $x$  in both images, which is much higher

than expected from the  $\text{MnO}_2$  planes. Indeed, it suggests that Mn has been substituted by a much heavier atom, even heavier than La. Strikingly, the intensity of the first atomic plane of the HZO structure, named  $i$  in Fig. 1, is lower than expected, which implies that the concentration of the heavy Hf ( $Z_{\text{Hf}} = 72$ ) and, to an extent, Zr ( $Z_{\text{Zr}} = 40$ ) is lower in this plane.

Further insights into this interface can be extracted by analyzing the spacings across the interface. For that, Gaussian curves were fitted to each atomic column in the observation plane of Fig. 1(c). Then the distances between the centers of first-neighbor Gaussians are taken as in-plane and out-of-plane spacings, and the averaged values are plotted as a function of the out-of-plane position, as shown in Fig. 1(d) (see a complete two-dimensional mapping of spacings across the interface in Fig. S4, Supplemental Material [37]). The results show that the in-plane and out-of-plane spacings are, for both HZO and LSMO layers, constant beyond the interface and coinciding with the expected values [26], 3.14 and 2.96 Å for HZO in-plane (distance equal to  $\frac{3}{2}$  of the distance between  $[-211]$  planes) and out-of-plane (111) spacings, respectively, and 2.76 and 3.9 Å for LSMO. Recall that the LSMO layer is fully strained on the STO substrate, thus replicating the in-plane lattice parameters of 3.9 Å for STO. However, the out-of-plane spacings at the interface deviate from the expected ones. Indeed, the distance between planes  $x$  and  $i$  (the first plane with HZO structure) is larger than the (111) HZO spacing (3.35 vs 2.96 Å), and the planes (half the distance between  $\text{La}_{2/3}\text{Sr}_{1/3}\text{O}$  planes), 2.3 vs 1.95 Å, respectively. It is worth noting that the out-of-plane spacings of the HZO twin variant shown in Fig. 1(b) across the interface follow the same trend (spacings profiles not shown here). These results show the presence of a sharp interface between such dissimilar structures, as opposed to the presence of a strain gradient in interfaces involving different perovskites such as  $\text{LaAlO}_3/\text{STO}$  [38].

To reveal the chemistry at the interface, we used EELS to obtain chemical maps with atomic resolution. Figure 2(a) shows a  $Z$ -contrast image of the interface. Figures 2(b)–2(f) show elemental maps of La- $M$ , Sr- $L$ , Mn- $L$ , Hf- $M$ , and Zr- $L$  edges, respectively, from an EELS image that was acquired simultaneously with the  $Z$ -contrast image. The atomic resolution elemental maps reveal that the last plane that can be considered chemically LSMO is a  $\text{La}_{0.67}\text{Sr}_{0.33}\text{O}$  plane. Likewise, different areas within the TEM specimen as well as different TEM specimens were inspected by EELS; they all revealed  $\text{La}_{0.67}\text{Sr}_{0.33}\text{O}$  to be the last plane with LSMO chemical composition. However, the termination of the STO substrate is mostly  $\text{TiO}_2$  terminated (Fig. S5, Supplemental Material [37]), and therefore, LSMO is expected to be primarily  $\text{MnO}_2$ , with minor areas having  $\text{La}_{0.67}\text{Sr}_{0.33}\text{O}$  termination [27,28]. Hence, the Mn expected to be present at the upper surface of LSMO has been substituted by Hf/Zr atoms, as sketched in Fig. 2(g), although in the  $A$ -terminated areas, the Hf/Zr is added as a metal in the  $B$  site of the perovskite. In addition, the dimmer intensity of the first atomic plane shown by the Hf and Zr elemental maps suggests a lower concentration of these two elements right at the HZO/LSMO interface. These results account for the contrast observed in planes  $x$  and  $i$  of the  $Z$ -contrast images shown in Fig. 1 and prove

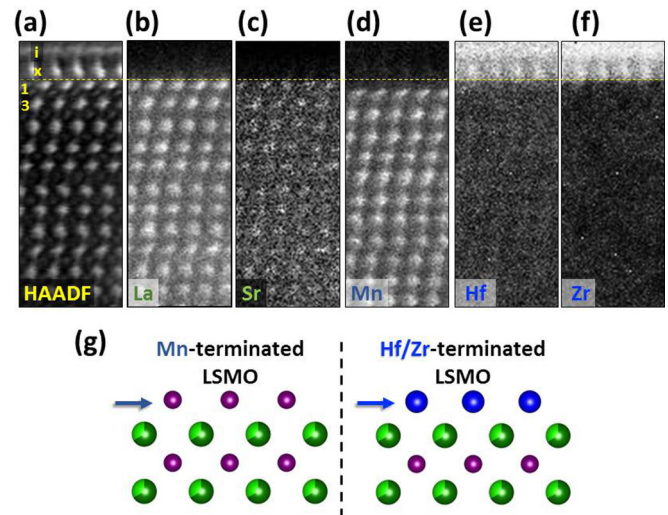


FIG. 2. (a) High-angle annular dark field (HAADF) image acquired simultaneously with the electron energy loss spectrum (EELS) image dataset along the  $[100]$  zone axis. (b)–(f) Elemental maps of La- $M$ , Sr- $L$ , Mn- $L$ , Hf- $M$ , and Zr- $L$  edges, respectively. (g) Sketch of the uppermost region of the LSMO layer illustrating the substitution of the terminating Mn plane by Hf/Zr cations. Mn (purple), Hf/Zr (blue), La (dark green), and Sr (light green) atoms are shown.

that a chemical reconstruction takes place at the HZO/LSMO interface.

Similar features are observed at the  $m$ -HZO/LSMO interface, with Hf/Zr occupying the Mn sites in layer  $x$ . However, HAADF images and EELS elemental maps of this interface show that the content of La and Hf/Zr in layers 1 and  $x$ , respectively, are lower (see Fig. S2, Supplemental Material [37]).

EELS also allows us to track changes in the electronic structure across the interface. It is well known that Mn- $L$  and O- $K$  edges are sensitive to changes in bonding, coordination, and the oxidation state of Mn [39]. Figure 3 shows the Mn- $L$  and O- $K$  edges from spectra acquired plane by plane [Figs. 3(a) and 3(e)], starting far below the interface until the HZO layer [Fig. 3(c)]. The Mn- $L$  edge includes the  $L_3$  and  $L_2$  white lines at onset energies of  $\sim 640$  and  $650$  eV, respectively. The intensity ratio of the  $L_3$  and  $L_2$  lines of the Mn- $L_{23}$  edge (the  $L_{23}$  ratio) correlates with the oxidation state of Mn [39]. The measured Mn- $L_{23}$  ratio is close to that of the LSMO compound, with a mix of  $\text{Mn}^{+2}$  and  $\text{Mn}^{+3}$  [39]. More importantly, the Mn- $L_{23}$  ratio remains unchanged on moving toward the interface, see Figs. 3(a) and 3(b). Hence, Mn does not change its oxidation state when approaching the HZO layer.

Regarding the O- $K$  edge [Fig. 3(e)], it shows a rather abrupt transition at the heterointerface, in agreement with the abrupt structural and chemical variations shown in Figs. 1 and 2. Within the LSMO layer, the O- $K$  edge shows a prepeak with an energy onset at  $\sim 527$  eV. The prepeak disappears after the interface between LSMO and HZO, as shown in Fig. 3(e). This is not the only change that takes place in the O- $K$  edge prepeak, as its intensity decreases in the uppermost Mn plane as well; see Fig. 3(f), where two O- $K$  edge spectra are compared, one from plane 1 and one from the lowermost  $\text{MnO}_2$  plane shown [plane 8 in Fig. 3(c)]. This

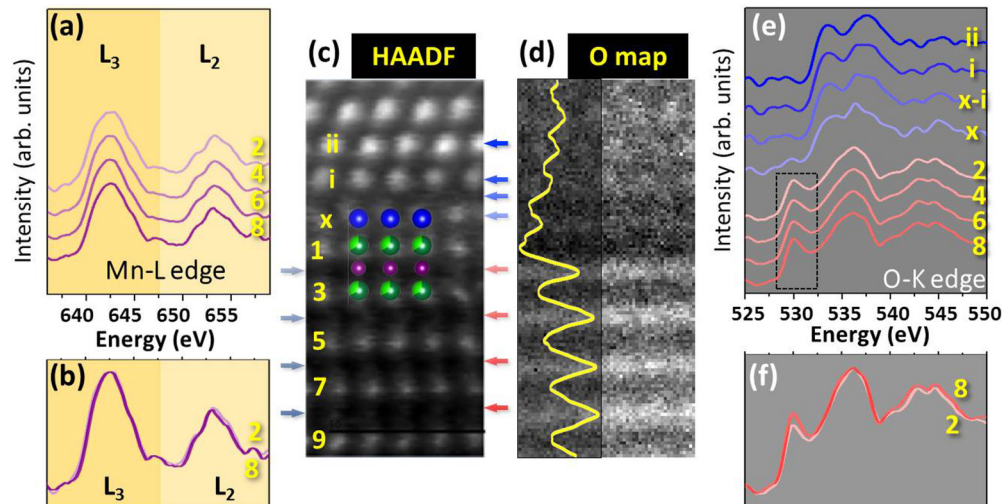


FIG. 3. Change of electronic fine structure across the LSMO/o-HZO heterointerface tracked using row-averaged (a) Mn-L edge and (e) O-K edge. (b) and (f) Superimposed spectra of the uppermost (2) and lowermost (8)  $\text{MnO}_2$  planes of Mn-L and O-K edges, respectively. (c) The high-angle annular dark field (HAADF) image (acquired along the  $[110]$  LSMO zone axis) from where spectra in (a) and (e) have been extracted, with the cation model structure superimposed [Mn (purple), Hf/Zr (blue), La (dark green), and Sr (light green)]. The colors of the spectra in (a), (b), (e) and (f) and of the arrows in (c) indicate the element analyzed in each atomic plane, with Hf/Zr in blue, O in red, and Mn in purple. The intensity ratio of the O prepeak (at 527 eV) and the main peak (at 535 eV) is  $\sim 0.3$  in the layers further from the interface, while this ratio becomes smaller ( $\sim 0.2$ ) at the interface, as shown in (f). (d) O elemental map across the LSMO/o-HZO heterointerface, and the corresponding intensity profile (yellow background) shows a smaller O signal at the interface, indicating that a smaller quantity of O is present. The O map in (d) was obtained by integrating the O-K in each pixel from  $\sim 527$  to  $\sim 540$  eV.

prepeak is sensitive to the partially filled  $2p$  states of oxygen, which are hybridized with  $3d$  states of manganese. Therefore, its variation in intensity is signaling either the presence of oxygen vacancies or transfer of electrons from Hf/Zr found in the perovskite plane  $x$ , or both, although the EELS oxygen elemental map in Fig. 3(d) reveals a weaker oxygen signal at the interface (especially at plane  $x$ ), indicating that oxygen is less abundant at the interface (see also Fig. S6, Supplemental Material [37]). The evolution of the fine structure as a function of the probe position can be obtained using a combination of DFT calculations and simulations based on dynamical scattering theory [40,41]. However, given the lack of a precise atomic model of the HZO/LSMO interface, such simulations are unfeasible. Our EELS experiments suggest the unambiguous presence of oxygen vacancies based on the total lower signal at the interface and the lower O prepeak intensity.

From the STEM experiments, we observe that the  $\text{MnO}_2$ -terminated surface layer of LSMO undergoes a chemical reconstruction; specifically, Mn atoms are substituted by Hf/Zr atoms. The LSMO top surface is expected to exhibit  $\text{MnO}_2$  termination [27,28], provided that the STO is mostly  $\text{TiO}_2$  terminated, and the stoichiometry is maintained in films grown by pulsed laser deposition (Fig. S5, Supplemental Material [37]). Instead, we find Hf/Zr atoms at the said layer. Moreover, an oxygen deficiency is detected at the interface, which indicates that the substitution of Mn atoms by Hf occurs under oxygen deprivation conditions. The presence of oxygen vacancies at the interface may also be relevant during the ferroelectric switching and screening [42,43], and electroresistance [6,44]. Interfacial reconstructions leading to the formation of a hybrid atomic plane bridging two dissimilar structures have been reported to allow for heteroepitaxy

of dissimilar oxides as binary oxides on perovskites [45]. These results rule out the presence of a tetragonal HZO phase at the LSMO/o-HZO interface of the explored specimen—the two atomic planes under the o-HZO structure contain La/Sr (plane 1) and Hf/Zr (plane  $x$ ) cations at the perovskite  $A$  and  $M$  sites, respectively—contrary to what has been previously reported in an equivalent heterostructure [19]. Furthermore, the HZO cation sublattice shows structural features incompatible with the tetragonal phase [46,47], see Fig. S7 of the Supplemental Material [37]. In brief, Fig. S7 shows that both the spacings and angles between atomic columns on the observation plane (corresponding to the Hf/Zr cation sublattice) reveal the expected “breathing” (periodic larger and smaller spacings and angles) of the orthorhombic phase, ruling out the presence of the tetragonal phase at the interface.

The large dissimilarity between the structure of HZO and LSMO results in a complex heterointerface that involves thousands of atoms [26] and prohibits the simulation of the heterointerface and extraction of its energy and electronic structure using DFT calculations. Instead, to understand the driving force for Hf substitution at the  $\text{MnO}_2$  layer, we have simulated the initial growth process and compared the energetics of  $\text{HfO}_x$  ( $x = 0, 1, 2$ ) clusters deposited as adatoms on  $\text{MnO}_2$  as opposed to Hf substituting Mn. More complex  $\text{HfO}_x$  clusters ( $x > 2$ ) on the  $\text{MnO}_2$  surface are beyond the scope of this paper due to computational limitations. The adsorption and substitution of Hf, HfO, and  $\text{HfO}_2$  on  $\text{MnO}_2$  are shown using atomic models in Figs. 4(a)–4(c), respectively. For classification, the structures with the Hf adatom on the surface and Hf substituting Mn at the  $\text{MnO}_2$ -terminated layer are referred to as Hf-A and Hf-E, respectively. The corresponding

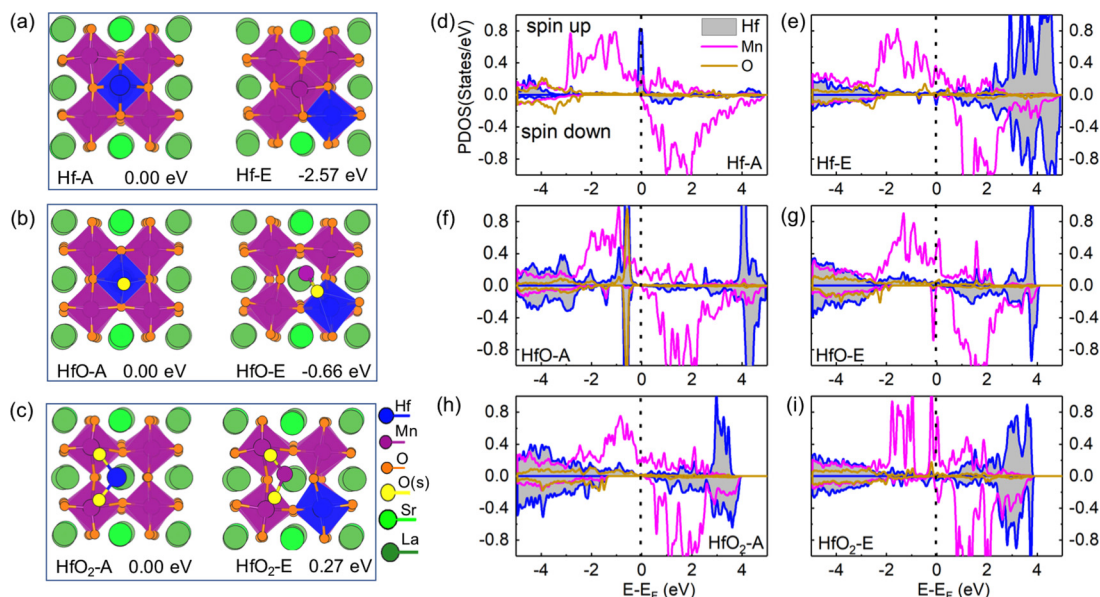


FIG. 4. (a)–(c) Top view of  $\text{La}_{0.75}\text{Sr}_{0.25}\text{MnO}_3$  slabs with Hf (Hf-A), HfO (HfO-A), or  $\text{HfO}_2$  (HfO<sub>2</sub>-A) clusters adsorbing on the  $\text{MnO}_2$ -terminated surface, left panel, and the Hf atom exchanging position with a surface Mn atom and getting embedded in the LSMO matrix (Hf-E, HfO-E, and HfO<sub>2</sub>-E), right panel. The conformations are represented by ball-and-stick models. Oxygen atoms adsorbing on the LSMO surface are labeled as O(s). The relative energies with reference to the  $\text{HfO}_x$ -A configurations are also shown. (d)–(i) Spin-polarized, atom-projected density of states (PDOS) of surface atoms in Hf-A, Hf-E, HfO-A, HfO-E, HfO<sub>2</sub>-A, and HfO<sub>2</sub>-E configurations.

structures of HfO are labeled as HfO-A and HfO-E, and that of  $\text{HfO}_2$  as HfO<sub>2</sub>-A and HfO<sub>2</sub>-E, respectively. For the adatom clusters, we find that the Hf atom tends to adsorb at the center of four neighboring Mn atoms of the  $\text{MnO}_2$  surface. Subsequently, we exchange the positions of the Hf adatom and a Mn atom of the surface to get the Hf-E, HfO-E, and HfO<sub>2</sub>-E configurations.

For a single Hf atom, we find that the Hf-Mn exchange (Hf-E configuration) lowers the total energy by 2.57 eV from the Hf-A configuration, as shown in Fig. 4(a). Therefore, there is a significant thermodynamic driving force for the formation of Hf-E from Hf-A. To understand this substitution, we analyze the electronic structure of the two configurations. The atom-projected density of states (PDOS) of the adatom and the top layer of LSMO for both Hf-A and Hf-E configurations are shown in Figs. 4(d) and 4(e), respectively. We find that the adsorption of Hf on the surface of  $\text{MnO}_2$  results in large, localized states around the Fermi energy, and these states are primarily derived from the Hf adatom. It indicates that Hf chemisorption induces surface dangling bonds, which leads to the higher energy of the Hf-A configuration. The electronic structure of the Hf-E configuration in Fig. 4(e) shows that the Hf-Mn exchange leads to a significant reduction of the Hf states near the Fermi energy due to the passivation of the dangling bonds. We have also analyzed the tendency for the formation of oxygen vacancy at the  $\text{MnO}_2$  surface on adsorption of Hf and the Hf-Mn exchange. The results are shown in Fig. S9 (Supplemental Material [37]). The results are consistent with Hf-A and Hf-E without any oxygen vacancies.

The difference in the electronic structure of the Hf-A and Hf-E configurations and the passivation of the dangling bonds with  $\text{Hf}_{\text{Mn}}$  substitution can be further understood from an

analysis of the surface charges based on nominal oxidation states. The nominal oxidation state of Mn in  $\text{La}_{0.67}\text{Sr}_{0.33}\text{MnO}_3$  is +3.33. In bulk, the two oxygen in a  $\text{Mn}^{+3.33}\text{O}_2^{-2}$  unit need four electrons, and Mn only donates 3.33  $e$ , so  $\text{Mn}^{+3.33}\text{O}_2^{-2}$  plane has a charge of +0.67 per unit cell. Similarly, the  $\text{La}_{0.67}^{+3}\text{Sr}_{0.33}^{+2}\text{O}^{-2}$  plane has a net charge of −0.67 per unit cell. Along the [001] direction in bulk LSMO, each  $\text{La}_{0.67}\text{Sr}_{0.33}\text{O}$  plane can be assumed as donating 0.335  $e$ /unit cell to its two adjacent  $\text{MnO}_2$  layers. The  $\text{MnO}_2$ -terminated surface, therefore, has a charge of +0.335 per unit cell, as it receives 0.335  $e$ /unit cell from only the underlying  $\text{La}_{0.67}\text{Sr}_{0.33}\text{O}$  layer. There are 4  $\text{MnO}_2$  units in the termination layer of the supercell; hence, the total surface charge is +1.34. The preferred oxidation state of Hf is +4. Hence, the substitution of  $\text{Mn}^{+3.33}$  by  $\text{Hf}^{+4}$  in  $\text{MnO}_2$  contributes an extra 0.67  $e$  for the entire ( $2 \times 2$ )  $\text{MnO}_2$  layer, reducing the total surface charges from +1.34 to +0.67 for the  $\text{MnO}_2$  layer. A Bader charge analysis [48]—that partitions the valence electrons to atoms using a zero-flux surface where the electron density is minimum—of the two configurations supports these results. We find that, with the substitution of Mn by Hf in Hf-E, the Bader charge of the termination layer greatly reduces to 0.13  $e$  from 1.10  $e$  in Hf-A (Table I).

Apart from Hf on top of the  $\text{MnO}_2$  layer, we have also analyzed the energetics of HfO and  $\text{HfO}_2$  clusters on  $\text{MnO}_2$ -terminated LSMO [Figs. 4(b) and 4(c)]. For molecular HfO adsorption, its results are like a Hf atom with the HfO-E configuration being 0.66 eV lower in energy than the HfO-A configuration. The mechanisms involved are like that of a Hf atom. HfO chemisorption induces surface dangling bonds in HfO-A and drives its energy higher [Fig. 4(f)]. Hf-Mn exchange leads to a significant reduction of the Hf states near the Fermi energy due to passivation of the dangling

bonds [Fig. 4(g)] and lowers the energy of the corresponding structure.

The behavior of the  $\text{HfO}_2$  cluster on  $\text{MnO}_2$ -terminated LSMO [Fig. 4(c)] is different from that of Hf and HfO molecules, with the  $\text{HfO}_2$ -A configuration being lower in energy by 0.27 eV from the  $\text{HfO}_2$ -E configuration. The reason for the different behavior of  $\text{HfO}_2$  is that the  $\text{HfO}_2$  cluster adsorbed on the  $\text{MnO}_2$  surface does not have any surface dangling bonds, as observed from the density of states of Hf in Fig. 4(h). The exchange between Hf and Mn does not lead to any significant charge rebalance at the surface (Table I). Moreover, in the  $\text{HfO}_2$ -E configuration, surface Mn-O bonds are partly broken due to the embedding of Hf (see the increase in Mn-O bond lengths in Fig. S8, Supplemental Material [37]). These broken bonds induce large, localized states near the Fermi energy [Fig. 4(i)] and increase the energy of the corresponding structure.

The variation in adsorption energy of Hf, HfO, and  $\text{HfO}_2$  on LSMO with respect to the oxygen chemical potential are given in Fig. S8 in the Supplemental Material [37]. It is observed that Hf-E is the most stable configuration when  $\mu_{\text{O}} < -6.99$  eV, i.e., under intermediate to Hf-rich (O-poor) growth conditions spanning a large range of  $\mu_{\text{O}}$  values. For a small range of  $-6.99$  eV  $< \mu_{\text{O}} < -6.44$  eV, we find HfO-E to be most stable. When  $\mu_{\text{O}} > -6.44$  eV, i.e., under oxygen-rich conditions,  $\text{HfO}_2$ -A becomes the most stable configuration on surface  $\text{MnO}_2$ . These results showing the stability of Hf-E over a large range of  $\mu_{\text{O}}$  values support the experimentally observed reduction in the EELS signal of the O-K edge at the interface due to formation of oxygen vacancies.

#### IV. CONCLUSIONS

In conclusion, the chemical and structural features of the HZO/LSMO heterointerface that allows epitaxial growth of ferroelectric HZO on perovskites have been revealed. Atomic resolution HAADF images and elemental maps show the chemical reconstruction of the  $\text{MnO}_2$ -terminated surface of

LSMO occurs during the epitaxial growth of HZO on the LSMO, which is supported by DFT calculations of total energy and electronic structure. The reconstruction consists of the substitution of the Mn cations of the  $\text{MnO}_2$  interface with HZO by a mixture of Hf/Zr atoms, with Hf/Zr occupying the sites of the Mn in the LSMO perovskite. Such a reconstruction occurs under oxygen deprivation conditions. These results are a critical step toward understanding the decisive role of the LSMO buffer in the stabilization of the ferroelectric phase in thin films of (Hf, Zr) $\text{O}_2$ . It is expected to encourage further studies owing to the critical role the interface plays on both the stabilization of the ferroelectric phase and its switching.

#### ACKNOWLEDGMENTS

Financial support from the Spanish Ministry of Science, Innovation and Universities, through the “Severo Ochoa” Programme for Centres of Excellence in R&D (SEV-2015-0496) and MAT2017-85232-R (AEI/FEDER, EU), PID2020-112548RB-I00 (AEI/FEDER, EU) and PID2019-107727RB-I00 (MINECO/FEDER, EU) projects, and from Generalitat de Catalunya (2017 SGR 1377) is acknowledged. S.E. acknowledges the Spanish Ministry of Economy, Competitiveness and Universities for his Ph.D. contract (SEV-2015-0496-16-3) and its cofunding by the ESF. S.E.’s work has been done as a part of his Ph.D. program in Materials Science at Universitat Autònoma de Barcelona. The electron microscopy performed at ORNL was supported by the Materials Sciences and Engineering Division of Basic Energy Sciences of the Office of Science of the U.S. Department of Energy. The work at Washington University was supported by the National Science Foundations (NSF) through Grant No. DMR-1931610 (T.C.) and No. DMR-1806147 (R.M.). This paper used the computational resources of the Extreme Science and Engineering Discovery Environment (XSEDE), which is supported by NSF ACI-1548562. Project supported by a 2020 Leonardo Grant for Researchers and Cultural Creators, BBVA Foundation. I.F. acknowledges Ramón y Cajal contract RYC-2017-22531.

- 
- [1] H. J. Lee, M. Lee, K. Lee, J. Jo, H. Yang, Y. Kim, S. C. Chae, U. Waghmare, and J. H. Lee, Scale-free ferroelectricity induced by flat phonon bands in  $\text{HfO}_2$ , *Science* **369**, 1343 (2020).
  - [2] S. S. Cheema *et al.*, Enhanced ferroelectricity in ultrathin films grown directly on silicon, *Nature* **580**, 478 (2020).
  - [3] J. Junquera and P. Ghosez, Critical thickness for ferroelectricity in perovskite ultrathin films, *Nature* **422**, 506 (2003).
  - [4] T. S. Böscke, J. Müller, D. Bräuhäus, U. Schröder, and U. Böttger, Ferroelectricity in hafnium oxide thin films, *Appl. Phys. Lett.* **99**, 102903 (2011).
  - [5] Y. Wei, S. Matzen, T. Maroutian, G. Agnus, M. Salverda, P. Nukala, Q. Chen, J. Ye, P. Lecoeur, and B. Noheda, Magnetic Tunnel Junctions Based on Ferroelectric  $\text{Hf}_{0.5}\text{Zr}_{0.5}\text{O}_2$  Tunnel Barriers, *Phys. Rev. Appl.* **12**, 031001(R) (2019).
  - [6] M. C. Sulzbach, S. Estandía, X. Long, J. Lyu, N. Dix, J. Gàzquez, M. F. Chisholm, F. Sánchez, I. Fina, and J. Fontcuberta, Unraveling ferroelectric polarization and ionic contributions to electroresistance in epitaxial  $\text{Hf}_{0.5}\text{Zr}_{0.5}\text{O}_2$  Tunnel Junctions, *Adv. Electron. Mater.* **6**, 1900852 (2020).
  - [7] M. C. Sulzbach, S. Estandía, J. Gàzquez, F. Sánchez, I. Fina, and J. Fontcuberta, Blocking of conducting channels widens window for ferroelectric resistive switching in interface-engineered  $\text{Hf}_{0.5}\text{Zr}_{0.5}\text{O}_2$  tunnel devices, *Adv. Funct. Mater.* **30**, 2002638 (2020).
  - [8] E. Yurchuk, J. Müller, R. Hoffmann, J. Paul, D. Martin, R. Boschke, T. Schlösser, S. Müller, S. Slesazeck, R. Van Bentum, M. Trentzsch, U. Schröder, and T. Mikolajick,  $\text{HfO}_2$ -based ferroelectric field-effect transistors with 260 nm channel length and long data retention, in *2012 4th IEEE International Memory Workshop* (IEEE, Milan, 2012), pp. 1–4.
  - [9] M. H. Park, Y. H. Lee, T. Mikolajick, U. Schroeder, and C. S. Hwang, Review and perspective on ferroelectric  $\text{HfO}_2$ -based thin films for memory applications, *MRS Commun.* **8**, 795 (2018).

- [10] M. H. Park, Y. H. Lee, H. J. Kim, Y. J. Kim, T. Moon, K. Do Kim, J. Müller, A. Kersch, U. Schroeder, T. Mikolajick, and C. S. Hwang, Ferroelectricity and antiferroelectricity of doped thin HfO<sub>2</sub>-based films, *Adv. Mater.* **27**, 1811 (2015).
- [11] J. Müller, U. Schröder, T. S. Böske, I. Müller, U. Böttger, L. Wilde, J. Sundqvist, M. Lemberger, P. Kücher, T. Mikolajick, and L. Frey, Ferroelectricity in yttrium-doped hafnium oxide, *J. Appl. Phys.* **110**, 114113 (2011).
- [12] J. Müller *et al.*, Ferroelectric hafnium oxide: a CMOS-compatible and highly scalable approach to future ferroelectric memories, in *2013 IEEE International Electron Devices Meeting* (IEEE, Washington DC, 2013), pp. 10.8.1–10.8.4.
- [13] J. Müller, T. S. Böske, U. Schröder, S. Mueller, D. Bräuhäus, U. Böttger, L. Frey, and T. Mikolajick, Ferroelectricity in simple binary ZrO<sub>2</sub> and HfO<sub>2</sub>, *Nano Lett.* **12**, 4318 (2012).
- [14] T. Shimizu, K. Katayama, T. Kiguchi, A. Akama, T. J. Konno, and H. Funakubo, Growth of epitaxial orthorhombic YO<sub>1.5</sub>-substituted HfO<sub>2</sub> thin film, *Appl. Phys. Lett.* **107**, 032910 (2015).
- [15] K. Katayama, T. Shimizu, O. Sakata, T. Shiraishi, S. Nakamura, T. Kiguchi, A. Akama, T. J. Konno, H. Uchida, and H. Funakubo, Orientation control and domain structure analysis of {100}-oriented epitaxial ferroelectric orthorhombic HfO<sub>2</sub>-based thin films, *J. Appl. Phys.* **119**, 134101 (2016).
- [16] T. Li, N. Zhang, Z. Sun, C. Xie, M. Ye, S. Mazumdar, L. Shu, Y. Wang, D. Wang, L. Chen, S. Ke, and H. Huang, Epitaxial ferroelectric Hf<sub>0.5</sub>Zr<sub>0.5</sub>O<sub>2</sub> thin film on a buffered YSZ substrate through interface reaction, *J. Mater. Chem. C* **6**, 9224 (2018).
- [17] J. Lyu, I. Fina, J. Fontcuberta, and F. Sánchez, Epitaxial integration on Si(001) of ferroelectric Hf<sub>0.5</sub>Zr<sub>0.5</sub>O<sub>2</sub> capacitors with high retention and endurance, *ACS Appl. Mater. Interfaces* **11**, 6224 (2019).
- [18] Z. Zhang, S. L. Hsu, V. A. Stoica, H. Paik, E. Parsonnet, A. Qualls, J. Wang, L. Xie, M. Kumari, S. Das, Z. Leng, M. McBriarty, R. Proksch, A. Gruverman, D. G. Schlom, L. Q. Chen, S. Salahuddin, L. W. Martin, and R. Ramesh, Epitaxial ferroelectric Hf<sub>0.5</sub>Zr<sub>0.5</sub>O<sub>2</sub> with metallic pyrochlore oxide electrodes, *Adv. Mater.* **33**, 2006089 (2021).
- [19] Y. Wei, P. Nukala, M. Salverda, S. Matzen, H. J. Zhao, J. Momand, A. S. Everhardt, G. Agnus, G. R. Blake, P. Lecoer, B. J. Kooi, J. Íñiguez, B. Dkhil, and B. Noheda, A rhombohedral ferroelectric phase in epitaxially strained Hf<sub>0.5</sub>Zr<sub>0.5</sub>O<sub>2</sub> thin films, *Nat. Mater.* **17**, 1095 (2018).
- [20] J. Lyu, I. Fina, R. Solanas, J. Fontcuberta, and F. Sánchez, Robust ferroelectricity in epitaxial Hf<sub>1/2</sub>Zr<sub>1/2</sub>O<sub>2</sub> thin films, *Appl. Phys. Lett.* **113**, 082902 (2018).
- [21] H. Y. Yoong, H. Wu, J. Zhao, H. Wang, R. Guo, J. Xiao, B. Zhang, P. Yang, S. J. Pennycook, N. Deng, X. Yan, and J. Chen, Epitaxial ferroelectric Hf<sub>0.5</sub>Zr<sub>0.5</sub>O<sub>2</sub> thin films and their implementations in memristors for brain-inspired computing, *Adv. Funct. Mater.* **28**, 1806037 (2018).
- [22] S. Estandía, N. Dix, J. Gazquez, I. Fina, J. Lyu, M. F. Chisholm, J. Fontcuberta, and F. Sánchez, Engineering ferroelectric Hf<sub>0.5</sub>Zr<sub>0.5</sub>O<sub>2</sub> thin films by epitaxial stress, *ACS Appl. Electron. Mater.* **1**, 1449 (2019).
- [23] S. Estandía, J. Gazquez, M. Varela, N. Dix, M. Qian, R. Solanas, I. Fina, and F. Sanchez, Critical effect of bottom electrode on ferroelectricity of epitaxial Hf<sub>0.5</sub>Zr<sub>0.5</sub>O<sub>2</sub> thin films, *J. Mater. Chem. C* **9**, 3486 (2021).
- [24] T. Li, M. Ye, Z. Sun, N. Zhang, W. Zhang, S. Inguva, C. Xie, L. Chen, Y. Wang, S. Ke, and H. Huang, Origin of ferroelectricity in epitaxial Si-doped HfO<sub>2</sub> films, *ACS Appl. Mater. Interfaces* **11**, 4139 (2019).
- [25] X. Sang, E. D. Grimley, T. Schenk, U. Schroeder, and J. M. Lebeau, On the structural origins of ferroelectricity in HfO<sub>2</sub> Thin Films, *Appl. Phys. Lett.* **106**, 162905 (2015).
- [26] S. Estandía, N. Dix, M. F. Chisholm, I. Fina, and F. Sánchez, Domain-matching epitaxy of ferroelectric Hf<sub>0.5</sub>Zr<sub>0.5</sub>O<sub>2</sub>(111) on La<sub>2/3</sub>Sr<sub>1/3</sub>MnO<sub>3</sub>(001), *Cryst. Growth Des.* **20**, 3801 (2020).
- [27] F. Sánchez, C. Ocal, and J. Fontcuberta, Tailored surfaces of perovskite oxide substrates for conducted growth of thin films, *Chem. Soc. Rev.* **43**, 2272 (2014).
- [28] P. Yu, W. Luo, D. Yi, J. X. Zhang, M. D. Rossell, C. H. Yang, L. You, G. Singh-Bhalla, S. Y. Yang, Q. He, Q. M. Ramasse, R. Erni, L. W. Martin, Y. H. Chu, S. T. Pantelides, S. J. Pennycook, and R. Ramesh, Interface control of bulk ferroelectric polarization, *Proc. Natl. Acad. Sci. USA* **109**, 9710 (2012).
- [29] R. Meyer, R. Waser, K. Prume, T. Schmitz, and S. Tiedke, Dynamic leakage current compensation in ferroelectric thin-film capacitor structures, *Appl. Phys. Lett.* **86**, 142907 (2005).
- [30] I. Fina, L. Fàbrega, E. Langenberg, X. Martí, F. Sánchez, M. Varela, and J. Fontcuberta, Nonferroelectric contributions to the hysteresis cycles in manganite thin films: a comparative study of measurement techniques, *J. Appl. Phys.* **109**, 074105 (2011).
- [31] G. Kresse and J. Furthmüller, Efficient iterative schemes for ab initio total-energy calculations using a plane-wave basis set, *Phys. Rev. B* **54**, 11169 (1996).
- [32] P. E. Blöchl, Projector augmented-wave method, *Phys. Rev. B* **50**, 17953 (1994).
- [33] J. P. Perdew, K. Burke, and M. Ernzerhof, Generalized Gradient Approximation Made Simple, *Phys. Rev. Lett.* **77**, 3865 (1996).
- [34] H. J. Monkhorst and J. D. Pack, Special points for Brillouin-zone integrations, *Phys. Rev. B* **13**, 5188 (1976).
- [35] H. Chen and S. Ismail-Beigi, Ferroelectric control of magnetization in La<sub>1-x</sub>Sr<sub>x</sub>MnO<sub>3</sub> manganites: a first-principles study, *Phys. Rev. B* **86**, 024433 (2012).
- [36] A. M. Glazer, The classification of tilted octahedra in perovskites, *Acta Cryst.* **28**, 3384 (1972).
- [37] See Supplemental Material at <http://link.aps.org/supplemental/10.1103/PhysRevMaterials.5.074410> for complementary measurements and calculations. Figure S1, polarization loop of HZO/LSMO/STO; Fig. S2, chemistry across the monoclinic-HZO/LSMO interface; Fig. S3, electronic structure across the monoclinic-HZO/LSMO interface; Fig. S4, interplanar spacings across the orthorhombic-HZO/LSMO interface; Fig. S5, chemistry of the lower LSMO/STO interface; Fig. S6, oxygen signal profile across the orthorhombic-HZO/LSMO interface; Fig. S7, mapping of the interplanar spacings inside a orthorhombic (HZO)-111 grain; Fig. S8; Mn-O bonds length calculations; and Fig. S9, formation of oxygen vacancies calculations.
- [38] J. Gazquez, M. Stengel, R. Mishra, M. Scigaj, M. Varela, M. A. Roldan, J. Fontcuberta, F. Sánchez, and G. Herranz, Competition between Polar and Nonpolar Lattice Distortions in Oxide Quantum Wells: New Critical Thickness at Polar Interfaces, *Phys. Rev. Lett.* **119**, 106102 (2017).



- [39] M. Varela, M. P. Oxley, W. Luo, J. Tao, M. Watanabe, A. R. Lupini, S. T. Pantelides, and S. J. Pennycook, Atomic-resolution imaging of oxidation states in manganites, *Phys. Rev. B* **79**, 085117 (2009).
- [40] M. P. Prange, M. P. Oxley, M. Varela, S. J. Pennycook, and S. T. Pantelides, Simulation of Spatially Resolved Electron Energy Loss Near-Edge Structure for Scanning Transmission Electron Microscopy, *Phys. Rev. Lett.* **109**, 246101 (2012).
- [41] B. D. Forbes, A. J. D'Alfonso, R. E. A. Williams, R. Srinivasan, H. L. Fraser, D. W. McComb, B. Freitag, D. O. Klenov, and L. J. Allen, Contribution of thermally scattered electrons to atomic resolution elemental maps, *Phys. Rev. B* **86**, 024108 (2012).
- [42] P. Nukala, M. Ahmadi, Y. Wei, S. de Graaf, E. Stylianidis, T. Chakraborty, S. Matzen, H. W. Zandbergen, A. Björling, D. Mannix, D. Carbone, B. Kooi, and B. Noheda, Reversible Oxygen Migration and Phase Transitions in Hafnia-Based Ferroelectric Devices, *Science* **372**, 630 (2021).
- [43] Y. M. Kim, A. Morozovska, E. Eliseev, M. P. Oxley, R. Mishra, S. M. Selbach, T. Grande, S. T. Pantelides, S. V. Kalinin, and A. Y. Borisevich, Direct observation of ferroelectric field effect and vacancy-controlled screening at the BiFeO<sub>3</sub>/La<sub>x</sub>Sr<sub>1-x</sub>MnO<sub>3</sub> interface, *Nat. Mater.* **13**, 1019 (2014).
- [44] C. Ferreyra, M. Rengifo, M. J. Sánchez, A. S. Everhardt, B. Noheda, and D. Rubi, Key Role of Oxygen-Vacancy Electromigration in the Memristive Response of Ferroelectric Devices, *Phys. Rev. Appl.* **14**, 044045 (2020).
- [45] X. Gao, S. Lee, J. Nichols, T. L. Meyer, T. Z. Ward, M. F. Chisholm, and H. N. Lee, Nanoscale selfflating for oxide epitaxy with large symmetry mismatch, *Sci. Rep.* **6**, 38168 (2016).
- [46] L. L. Tao, T. R. Paudel, A. A. Kovalev, and E. Y. Tsymbal, Reversible spin texture in ferroelectric HfO<sub>2</sub>, *Phys. Rev. B* **95**, 245141 (2017).
- [47] U. Schroeder, C. Richter, M. H. Park, T. Schenk, M. Pešić, M. Hoffmann, F. P. G. Fengler, D. Pohl, B. Rellinghaus, C. Zhou, C. C. Chung, J. L. Jones, and T. Mikolajick, Lanthanum-doped hafnium oxide: a robust ferroelectric material, *Inorg. Chem.* **57**, 2752 (2018).
- [48] W. Tang, E. Sanville, and G. Henkelman, A grid-based Bader analysis algorithm without lattice bias, *J. Phys. Condens. Matter* **21**, 084204 (2009).